Image Cover Sheet

CLASSIFICATION	SYSTEM NUMBER
UNCLASSIFIED	503452

TITLE

FAULT DETECTION AND FAULT RELATED PERFORMANCE DEGRADATION IN SONAR ARRAYS

System Number:

Patron Number:

Requester:

Notes:

DSIS Use only:

Deliver to:

Fault Detection and Fault Related Performance Degradation in Sonar Arrays

N.T. Allcott

Sonar Signal Processing Group, Defence Research Establishment Atlantic
P.O. Box 1012, 9 Grove St., Dartmouth, N.S., CANADA B2Y 3Z7

Abstract — It is desirable to maximize sonar gain against noise and interference in the prevailing underwater acoustic environment. Although significant emphasis is placed upon monitoring and modeling underwater acoustics for these purposes, little attention is paid to sensing the prevailing sonar configuration, especially deficiencies in the configuration arising from faults, design conditions, or improper operation. Yet, these deficiencies can degrade sonar performance as seriously as external environmental factors. In this paper, several techniques are examined for detecting fault related sonar configuration deficiencies and evaluating their effect on sonar performance. In particular, these analysis techniques are employed within a hierarchical framework that specifies the fault detection and performance evaluation methodology. The usefulness of this approach is demonstrated using both simulated data examples and real data gathered from towed array trials at sea.

1. INTRODUCTION

Sonar performance is predominantly affected by: (1) the underwater acoustic environment and (2) the sonar configuration. Significant effort has been expended in monitoring and modeling the underwater acoustic environment to estimate its effect on sonar performance [1]. Although an ideal sonar configuration is usually assumed for these purposes, in reality, configuration deficiencies such as faults, design conditions, or improper operation may invalidate these assumptions to the extent that sonar performance is significantly degraded from that expected. Many configuration deficiencies can be corrected or controlled, if identified. It would therefore be of value to include a fault detection and correction capability in the sonar to minimize performance loss due to these conditions.

Although substantial effort has been placed on addressing faults in areas such as VLSI, digital computation, telecommunications, and dynamic system control [2, 3], there are few results pertaining to sonar. Early fault analysis work in many of these areas focused on the use of redundancy and classical detection methods [4] applied at a single hierarchical level or sub-system in the overall system hierarchy. In this strategy, the fault analysis is performed at the sub-system in which the fault might occur. More modern strategies focus on detecting sub-system faults by applying fault analysis at higher levels of system hierarchy [3]. This allows detection of faults in many lower level hierarchical system components simultaneously, using a centralized algorithm. The advantage of this approach is that the cost related to the maintenance of a fault can readily be compared with the overall benefit of fault recovery to the system. Elaborate fault analysis schemes that cascade from high to lower hierarchical levels to gather more specific information about fault conditions, may then be realized on this basis.

For multi-sensor sonars, sensor fault analysis employing classical detection is straightforward due to the redundancy implicit in sensor arrays. This approach, however, provides only basic sensor fault detection capabilities and none of the more elaborate capabilities of the hierarchical approach. An early example of a hierarchical approach in this area, but one that is impractical for sonar, involves detecting element faults in a phased-array radar through model-based comparative analysis of the antenna outputs [5]. More applicable are the more recent results of Wagstaff [6, 7] detailing a multi-level hierarchical approach to sonar array fault analysis and the evaluation of sonar operational status.

During the course of this paper, a new hierarchical fault analysis strategy for sonar arrays is proposed. To familiarize the reader with the sonar fault problem and some of the reasoning and mathematics behind implementation of an analysis strategy, a number of items will be introduced in the next two sections.

2. THEORETICAL BACKGROUND

The functional structure of a passive sonar is shown in Figure 1 (a). The $J_1 \times N$ dimension sampled array sensor time series, $x_i(n)$, is processed by N-length FFTs to determine the Fourier transform of each sensor, $i = \{1,\ldots,J_1\}$, as follows,

$$X^{J_1 \times N} = FFT_{n=0}^{N-1}\left[x^{J_1 \times N}\right] \quad . \qquad (1)$$

A K-length temporal-spectral band of interest is then spatially processed by zero-extending the aperture (concatenate J_2 zero sensors) for the desired number of spatial estimates required and by applying FFT processing across the aperture:

$$B^{(J_1+J_2)\times K} = FFT_{b=0}^{(J_1+J_2)-1}\left[\underbrace{X^{J_1 \times K}}_{J_1}, \underbrace{0,0,\ldots,0}_{J_2}\right] \quad . \qquad (2)$$

The instantaneous power in a spectral bin, k, is computed simply as the squared magnitude of its Fourier transform,

$$P(k) = |X(k)|^2 .$$

Spectral power estimation involves averaging instantaneous power spectra over time. With a quantized process, this may be done either through an arithmetic average, $\hat{P}_A$, geometric average, $\hat{P}_G$, or median, $\hat{P}_M$. The median is known to provide the least bias in the estimate of the mean of a process when the corrupted sample content in the data is less than 50% of the total number of samples. The geometric

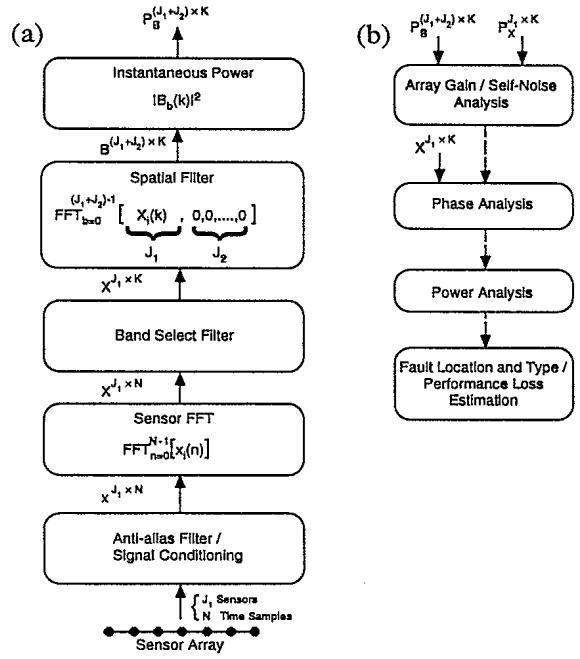

Figure 1. — (a) Functional structure of a passive sonar showing functional blocks and the resulting output data; (b) Hierarchical fault analysis processing structure. Input data specific to each hierarchical level block is indicated. The results of fault analysis at higher levels flow through to lower levels.

average has bias rejection that is similar to the median except for its increased bias sensitivity to outliers of magnitude smaller than unity. In comparison, the arithmetic average may be severely biased by all outliers.

The phase relationship of spectral estimates produced at the array sensors for the k-th temporal-spectral bin is determined by cross spectral density. Cross spectral density is estimated by averaging the conjugate product of sensor spectra for a bin, k, over M temporal snapshots such that the relationship between sensor pairs, (i, j), is of the form:

$$\hat{\Re}(k)_{ij} = \frac{\sum_{m=0}^{M-1} \Re(k)_{ij}}{M} \quad , \qquad \Re(k)_{ij} = X_i(k) X_j^*(k) \qquad . \quad (3)$$

Relative phases between adjacent sensors in the array can be computed by considering the $J_1 - 1$ terms of Equation (3) for which the phase difference, φ_{ij}, for $j = i \pm 1$, is simply computed as,

$$\varphi_{ij} = \tan^{-1}\left(\frac{imag(\hat{\Re}(k)_{ij})}{re(\hat{\Re}(k)_{ij})} \right) .$$

The overall performance of the sonar can be expressed in the generalized sonar equation,

$$SE = Max\{IL + TS, SL\} + AG - DT - \left[\sum_{p=1}^{P} TL_p + Max\{NL_S, NL_A, RL\} \right] \quad . \quad (4)$$

where IL is the acoustic illuminating level of an active system; TS, the target echo return strength; SL, the target source level; AG, the array gain; DT, the detection threshold; TL_P, the transmission loss over the p-th propagation path ($P = \{1,2\}$); and $Max\{NL_S, NL_E, RL\}$, the noise masking level dominated by either self-noise, environmental noise, or reverberation, respectively. The difference between the processed target acoustic energy and the combination of transmission loss, noise, and interference equals the signal-to-noise ratio in the detection bin, SE. The detection threshold, DT, is set such that when SE is zero, the desired criterion for probability of detection and false alarm are achieved (usually 50% probability of detection and a very small probability of false alarm, say 1 in 10,000). All quantities are in decibels referenced to 1 μPa/cm^2. For the passive sonar considered in Figure 1 (a), the term P is unity and the terms RL and $IL + TS$ do not apply.

Degradation in sonar performance is associated with a reduction in the value of signal excess, SE, available for detection as a result of one or more of the parameters of Equation (4) having been altered. Performance degradation due to sonar configuration deficiencies is attributed to the sonar controllable parameters of Equation (4), namely, reduction in array gain, AG, and/or increase in self-noise, NL_S. All other terms in Equation (4) refer to factors external to the sonar.

3. Faults and Sonar Performance Degradation

The hierarchy of the sonar processing structure and the ordering of its functional components may be studied with reference to Figure 1 (a). The highest level of functionality in the sonar is the detection of spectral energy from a target of interest at the sonar output. The lower level sub-systems, from input to output, essentially support this high-level functionality within the sonar processing hierarchy.

Hierarchical Fault Analysis

The effects of faults that occur within lower level sub-systems of the sonar may be observed at higher levels and eventually at the sonar output. By observing the magnitude of the sonar performance degradation at these higher levels (including the sonar output), the significance of any fault in a lower level sub-system can be ascertained. Figure 1 (b) outlines the hierarchical fault analysis strategy under consideration. In this strategy, fault analysis flows down through the hierarchy from the high to the low levels. The details of the fault tests identified in Figure 1 (b) are described in the next section.

Evaluating Fault Related Performance Loss

Using information gathered during the fault analysis, it is possible to estimate the performance loss due to faults separately from that due to the acoustic

environment. As faulty sensors will have significant levels of self-noise, gain error, or phase error compared to other sensors in the array, the coherence function across the aperture of a faulty sensor array will exhibit discontinuities. This is markedly different than the smoothness of the coherence function characteristic of acoustic field pressures measured by a sensor array without faults, and thereby allows the fault sites to be identified quite accurately. Performance loss attributed to such faulty arrays can be estimated using a simple, idealized perturbation model of the coherent spatial processing of the line-array sonar, based on the principle of superposition. Assuming a single narrowband arrival in 3-D isotropic noise, the output Signal-to-Noise Ratio (SNR) loss, ΔB is estimated as follows:

$$\Delta B = 10\log\left(\left[\frac{1}{J_1}\right]\left[\left|\sum_{i=0}^{J_1} G_i e^{j\Lambda_i}\right|^2 \Big/ \sum_{i=0}^{J_1} N_i^2\right]\right) \quad , \quad (5)$$

where; G_i, is the sensor gain error relative to the measured median sensor gain; Λ_i, the measured sensor phase error; and N_i, the measured excess in sensor noise relative to the median level of sensor noise. The loss in SNR at the system output, ΔB, directly reduces the signal excess, SE, and thereby provides a reasonably accurate estimate of the reduction in sonar detection performance due to detected faults.

4. Hierarchical Fault Analysis In Practice

To demonstrate the effectiveness of the proposed strategy, a data set will be subjected to the hierarchical fault analysis process depicted in Figure 1 (b). The computational tools and algorithms presented provide a minimum fault analysis capability within the hierarchical framework suggested. Other algorithms may be substituted if deemed necessary or advantageous.

The data are comprised of real towed line-array time series with hydrophone channel faults, but are further augmented with simulated faults to enhance the demonstration of fault processing at each level. The data are taken from a 32 sensor, 16-λ wavelength line-array, over a frequency range of $(5.88\,\lambda)^{-1}$ to D.C. The passive sonar processing is accomplished within 1 Hz narrowband temporal-spectral cells, generated from 50% temporally overlapped 1 second records of array sensor data, of which 100 records are made available. The spatial filter is a 256-point FFT applied across the zero-extended sensor aperture at each 1 Hz temporal-spectral bin. A temporal weighting of unity is used for the sensor FFTs. Hamming spatial shading is applied across the array aperture during spatial filtering.

Figure 2 (a) and (b) are greyscale plots of the arithmetically averaged, absolute value output of spectral estimators defined in Equations (1) (temporal spectra) and (2) (spatial spectra) when applied to the data. The dark triangular region in the center of Figure 2 (b) contains the acoustic power spectra. The lighter regions to the left and right contain the non-acoustic or self-noise power spectra. The importance of each of these regions will be explained shortly.

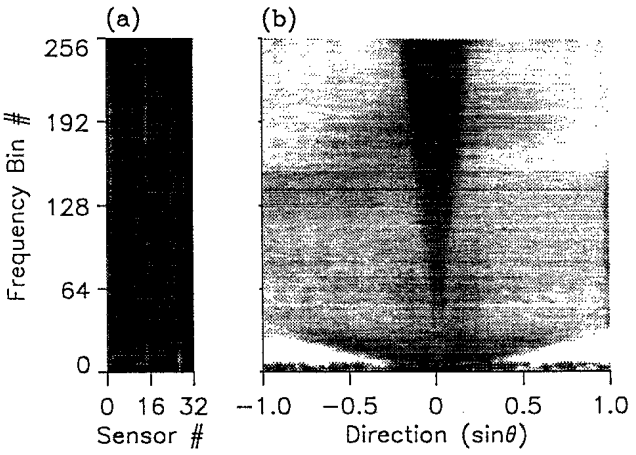

Figure 2. — (a) A greyscale plot of sensor powers (temporal spectra) as a function of frequency bin and sensor #; (b) A similar plot of spatial filter output power as a function of frequency bin # and spatial direction. Both greyscale plots were generated using equivalent greyscale parameters.

Array Gain Analysis

The loss in array gain at the sonar output due to faults or external conditions may be determined if one or more coherent sources are present. The existence of a coherent source is verified by detection at the sensor array prior to spatial filtering. The data required for this process are the array's best estimate of the acoustic field power and an estimate of the background noise power in the field. The field power estimate is obtained by taking a 2D median over all sensors and temporal records, represented as,

$$P_F^{1\times K} = \hat{P}_M\left[P_X^{J_1\times K\times M}\right]_{\rightarrow J_1 \atop \rightarrow M} \quad .$$

The noise background is estimated using a small, moving median smoothing window, W, over the acoustic field power estimate, as follows,

$$P_{FN}(k) = \hat{P}_M\left[P_F^{1\times K}\right]_{\rightarrow (W\cap K)\,@\,k} \qquad (6)$$

$$P_{FN}^{1\times K} = \left\{P_{FN}(0), P_{FN}(1), \ldots, P_{FN}(K)\right\} \quad .$$

Note that the smoothing window estimates noise relative to its center bin, k_c, and is defined in terms of the spectral bin set,

$$W = \left\{k \middle| k = k_c - \alpha, k_c - \alpha + 1, \ldots, k_c, \ldots, k_c + \alpha - 1, k_c + \alpha\right\}$$

$$\text{for} \qquad \alpha \le k_c \le K - \alpha$$

where α is a function of the window width, β, in spectral bins such that,

$$\alpha = \text{int}(\beta/2) \quad .$$

At the data edges, int($\beta/2$) extra edge points of value $P_F(0)$ for $0 \le k_c \le \alpha$ and $P_F(K-1)$ for $K-\alpha \le k_c \le K-1$ are used to allow smoothing at both ends of the temporal spectra. A coherent arrival at some bin, k_0, that is greater than 3 times (+5 dB) the noise background should be well observed in the spatial filter output. The direction of the arrival will correspond to the spatial estimate bin, $b = b_0$, containing the peak value of the spatial power estimate,

$$P_S^{(J_1+J_2)\times K} = \hat{P}_M\left[P_B^{(J_1+J_2)\times K\times M}\right]_{\to M} ,$$

for temporal-spectral bin k_0. The noise background at spatial bin b_0 is computed by applying the same median smoothing as used in Equation (6) over the temporal-spectral dimension of the spatial power estimates at equivalent direction spatial bins,

$$b_0' = \text{int}\left(\left[2b_0k + (J_1+J_2)(k_0-k)\right]/2k_0\right) \quad , \quad (7)$$

such that,

$$P_{BN}(k,b_0') = \hat{P}_M\left[P_S(b_0')^{1\times K}\right]_{\to (W\cap K)\,@\,k} \quad . \quad (8)$$

The loss in array gain may be computed directly from the following equation,

$$\Delta AG = 10\log\left(\left[{}^{P_S(k_0,b_0)}\!/_{P_F(k_0)}\right] \Big/ J_1\left[{}^{P_{BN}(k_0,b_0)}\!/_{P_{FN}(k_0)}\right]\right) ,$$

which is simply the logarithm of the ratio of signal gain to noise gain normalized by the optimum array gain. Again, a loss of 5 dB or more warrants further investigation. Results for the demonstration data set are provided in Table 1. The median smoothing window is such that β=17 temporal-spectral bins. Here, no synthetic faults were incorporated in the data. Only one coherent arrival was detected at the sensor array in bin $k_0 = 53$ as observed in Figure 2 (a). The arrival direction is 78° from the array axis.

SELF-NOISE ANALYSIS

Array self-noise propagates at wave velocities that are less than the speed of sound in water, c_w. In line-arrays, this "non-acoustic" energy may be observed in the spatially filtered output at steering delay rates of more than d/c_w, where d is intersensor separation. Comparing levels of non-acoustic noise with levels of "acoustic" noise (delay rates at most d/c_w), makes it possible to determine if self-noise is predominant. An ac ceptable measure of self-noise

$10\log(P_F(k_0))$	$10\log(P_{FN}(k_0))$	$10\log(P_S(k_0,b_0))$	$10\log(P_{BN}(k_0,b_0))$
20.46 dB	14.33 dB	19.03 dB	7.14 dB

Array Gain Loss ΔAG	Signal Gain Loss $10\log(P_S(k_0,b_0)/P_F(k_0))$	Noise Gain Loss $10\log(P_{BN}(k_0,b_0)/P_{FN}(k_0))-10\log(J_1)$
-9.295 dB	-1.43 dB	-7.865 dB

Table 1. — Results of array gain analysis.

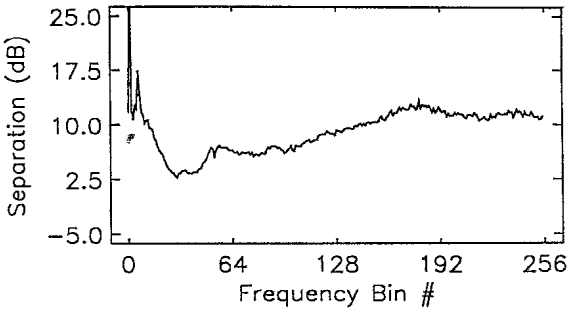

Figure 3. — A plot of self-noise / acoustic noise separation. At frequency bins less than $k = 180$ (low frequencies), separation diminishes. At frequency bins less than $k = 32$, the array is essentially omni-directional and the self-noise becomes more correlated, corrupting the acoustic beams significantly. Here, the ratio of the correlated and uncorrelated portions of self-noise are observed in the separation plot. The separation for the coherent arrival at $k = k_0 = 53$ is approximately 6 dB.

may be made as follows,

$$P_{SN}^{1\times K} = \hat{P}_M\left[P_S^{(J_1+J_2)\times K}\right]_{\to(\{\omega_f,\omega_a\}\cap(J_1+J_2))} ,$$

where $\{\omega_f, \omega_a\}$ are data selection windows covering 50% of the spatial estimates in the forward-endfire and aft-endfire non-acoustic regions at a single temporal-spectral bin. These selection regions are specifically defined as spatial bin sets:

$$\omega_f = \left\{b \middle| b = 0,1,\ldots,\text{int}\left((J_1+J_2)(1-(2dk/c_w))/4\right)\right\}$$

$$\omega_a = \left\{b \middle| b = \text{int}\left((J_1+J_2)(3+(2dk/c_w))/4\right)-1,\ \text{int}\left((J_1+J_2)(3+(2dk/c_w))/4\right),\ldots,(J_1+J_2)-1\right\} .$$

Acoustic noise is estimated from J_1 directions equally distributed within the acoustic region of the spatial filter power output, P_S. The spatial bins of equivalent direction for this purpose may be determined using Equation (7), where the J_1 directions are selected from the set,

$$b_0 = \left\{b \middle| b = \text{int}(J_2/2), \text{int}(J_2/2)+1,\ldots,\text{int}(J_2/2)+J_1-1\right\}$$

and where k_0 in Equation (7) is defined as,

$$k_0 = \left(c_w/2d\right)J_1/(J_1+J_2) \quad .$$

The resulting $J_1 \times K$ dimension directional acoustic spectra, $P_S(k,b_0')$, are subject to the same median filter smoothing as described in Equation (8). The minimum of the smoothed acoustic spectra is then selected at each temporal-spectral bin as follows:

$$P_{AN}(k) = \min\left(P_{BN}(k,b_0')\right) \quad .$$

Figure 3 is a plot of the logarithmic ratio of the spatial acoustic noise and self-noise estimates, $10\log(P_{AN}/P_{SN})$ for the demonstration data set with no synthetic faults. In self-noise dominated regions, the ratio is small, as may be observed at lower frequencies in Figure 3. The self-noise is

not dominant in the vicinity of the coherent arrival, where there is approximately 6 dB of separation between acoustic noise and self-noise.

SENSOR PHASE ANALYSIS

A line-array spatial filter estimates the level of acoustic energy arriving from an angular direction, θ, relative to array orientation by inserting delays at each sensor of $\tau_b = 2\pi b(d/c_w)\cos\theta, \quad b = \{0,\ldots,(J_1+J_2)-1\}$. A coherent source arrival from this direction will be coherently summed across the array aperture, providing gain over that of a single sensor. Conversely, incoherent source arrivals are averaged down relative to the single sensor. Maximum gain may only be achieved if the source is fully coherent over the aperture. The level of source coherence may be estimated from the following:

$$\wp^{J_1\times 1} = \hat{P}_M\left[re\left(S(k,\theta)\overline{\Re}(k)S^*(k,\theta)\right)^{J_1\times J_1}\right]_{\rightarrow J_1} \quad \text{where,}$$

$$S(k,\theta) = \left(diag\{1, e^{j2\pi k(d/c_w)\cos(\theta)},\ldots, e^{j2\pi k(d/c_w)(J_1-1)\cos(\theta)}\}\right)^{J_1\times J_1}$$

$$\text{and} \quad \overline{\Re}(k) = \left(\hat{\Re}(k)_{ij} \Big/ \left|\hat{\Re}(k)_{ij}\right|\right)^{J_1\times J_1}.$$

The coherence measure is simply the best mean estimate from the rows of the $J_1 \times J_1$ dimension, normalized and steered cross spectral density matrix, $\hat{\Re}(k)$, for any coherent arrival detectable at the sensor in a temporal-spectral bin, $k = k_0$. Figure 4 (a) is a plot of the coherence of the demonstration data set for the detected coherent arrival. Simulated faults include static phase errors of -100° and 40° added to sensors 5 and 11, respectively; and excesses of 5 dB and 8 dB (relative to median sensor noise at $k_0 = 53$) of self-noise added to sensors 20 and 23. It is observed that there is an overall coherence loss of about 20% due to incoherent effects in the data. At sensors 1, 5, 11, 14, 20, 23, and 26 the coherence has fallen noticeably from the norm. These discontinuities are characteristic of sensor faults. The actual faulty sensors are 1, 14, and 26. To determine if a fault is related to excess self-noise or phase error, the intersensor phase mean, μ_φ, and variance, $\sigma_\varphi{}^2$, are examined:

$$\mu_{\varphi_{ij}} = \tan^{-1}\left(\frac{imag(S(k,\theta)_{ij}\hat{\Re}(k)_{ij}S*(k,\theta)_{ij})}{re(S(k,\theta)_{ij}\hat{\Re}(k)_{ij}S*(k,\theta)_{ij})}\right)$$

$$\sigma^2_{\varphi_{ij}} = \frac{\sum_{m=0}^{M-1}\left(\tan^{-1}\left(\frac{imag(S(k,\theta)_{ij}\Re(k)_{ij}S*(k,\theta)_{ij})}{re(S(k,\theta)_{ij}\Re(k)_{ij}S*(k,\theta)_{ij})}\right)-\mu_{\varphi_{ij}}\right)^2}{M-1}.$$

Figure 4 (b) and (c) are plots of the mean phase and phase variance for adjacent sensor pairs in the demonstration data set as augmented with simulated faults. Note that the mean phase is subject to noticeable discontinuities at sensor pairs associated with all sensors exhibiting poor coherence in Figure 4 (a). The mean phases of the synthetic sensors with known static phase errors have been accurately estimated. The sensor variance is only discontinuous at sensor pairs related to sensors 1, 14, 20, 23, and 26. These correspond to noisy sensors. Those with known large static phase error, 5 and 11, do not exhibit large phase variance.

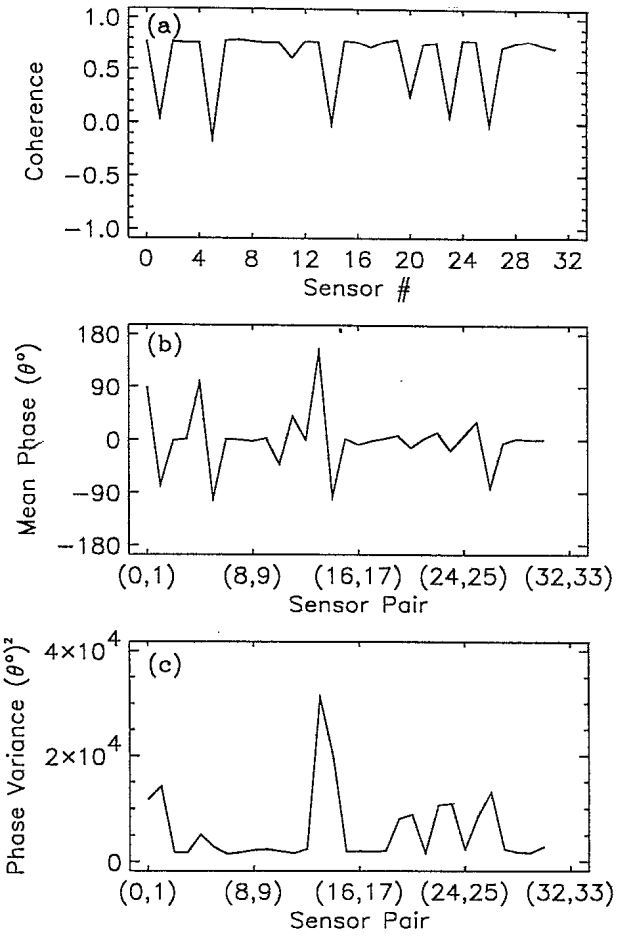

Figure 4. — (a) Sensor coherence as a function of sensor #. Sensors 1, 5, 11, 14, 20, 23, and 26 exhibit the characteristic faulty coherence discontinuity; (b) Mean phase of adjacent sensors. Note significant phase error in sensors 1, 5, 11, 14, and 26; and (c) Phase variance of adjacent sensors. Note that noisy sensors have significant variance. Sensors with static phase errors have a variance associated with their noise content.

DATA POWER ANALYSIS

In the lowest level of fault analysis, noisy sensor locations are corroborated and the potential for channel gain imbalance is determined through the use of Wagstaff's results [7]. In a properly functioning sonar, the power values observed in both the sensor temporal spectra and spatial filter output bins should be relatively well behaved over a suitable temporal ensemble. The existence of erratic levels in such power estimates indicates either excessive impulsive noise or intermittent operation. Wagstaff proposes two types of measurements for this situation that are of significant value. The first is concerned with the influence of outliers in a power estimation bin. Two $J_1 \times K$ dimension matrices, H_X and L_X, describe the bias in the sensor mean power estimate due to high and low level outliers, respectively:

$$H_X^{J_1\times K} = \frac{\hat{P}_A\left[P_X^{J_1\times K\times M}\right]_{\to M}}{\hat{P}_M\left[P_X^{J_1\times K\times M}\right]_{\to M}} \quad L_X^{J_1\times K} = \frac{\hat{P}_M\left[P_X^{J_1\times K\times M}\right]_{\to M}}{\hat{P}_G\left[P_X^{J_1\times K\times M}\right]_{\to M}} \quad .$$

Similar quantities, H_B, and L_B, may be calculated for spatial filter power estimates. A deviation from the median of more than a factor of 3 ($10\log$ of H_X, L_X, H_B, or $L_B > 5$ dB) is unacceptable [7]. Figure 5 (a) is a plot of the arithmetic mean, geometric mean, and median sensor power estimates in decibels at temporal-spectral bin $k = k_0$ for the demonstration data set without synthetic faults. Sensors with unacceptably high bias (where $10\log H_X > 5$ dB) are identified with small diamonds directly above. Sensor 26 is the only sensor indicated with this condition. At all sensors $10\log L_X < 5$ dB, hence, the low bias is acceptable. Figure 5 (b) shows a similar plot for spatial power. The high and low bias in the spatial spectra are acceptable in this case as both $10\log H_B$ and $10\log L_B$ are less than 5 dB for all spatial directions.

Wagstaff's second measure is concerned with how accurately sensors measure the predefined value $P_F(k_0)$. For each sensor the following estimates are computed,

$$\hbar(i,m) = 1, \left\{\frac{P_X(k_0,i,m)}{P_F(k_0)} > 3 \quad \ell(i,m) = 1, \left\{\frac{P_X(k_0,i,m)}{P_F(k_0)} < \frac{1}{3}\right.\right.$$

$$\hbar(i,m) = 0, \quad otherwise \qquad \ell(i,m) = 0, \quad otherwise \quad ,$$

and an average over the estimate vectors,

$$\overline{\hbar}^{J_1\times 1} = \hat{P}_A\left[\hbar^{J_1\times M}\right]_{\to M} \qquad \overline{\ell}^{J_1\times 1} = \hat{P}_A\left[\ell^{J_1\times M}\right]_{\to M} \quad ,$$

yields the desired result. The quantities, $\overline{\hbar}$ and $\overline{\ell}$, describe the fraction of time (ranging 0.0 to 1.0), over the M snapshots, a sensor measures the best estimate of the acoustic field power with an error in excess of 5 dB either higher ($\overline{\hbar}$) or lower ($\overline{\ell}$). Sensors exhibiting this behavior more than 50% (0.5) of the time are unacceptable. Figure 5 (c) is a plot of $\overline{\hbar}$ and $\overline{\ell}$ over the sensor array aperture at temporal-spectral bin $k = k_0$ for the demonstration data set without simulated faults. Sensors 1, 14, and 26 are observed to under-measure more often than the others. However, they are acceptable as the under-measure occurs less than 50% of the time. As all sensors are used to select the value $P_F(k_0)$, measures $\overline{\hbar}$ and $\overline{\ell}$ are viewed as a comparative assessment of sensor measurement quality.

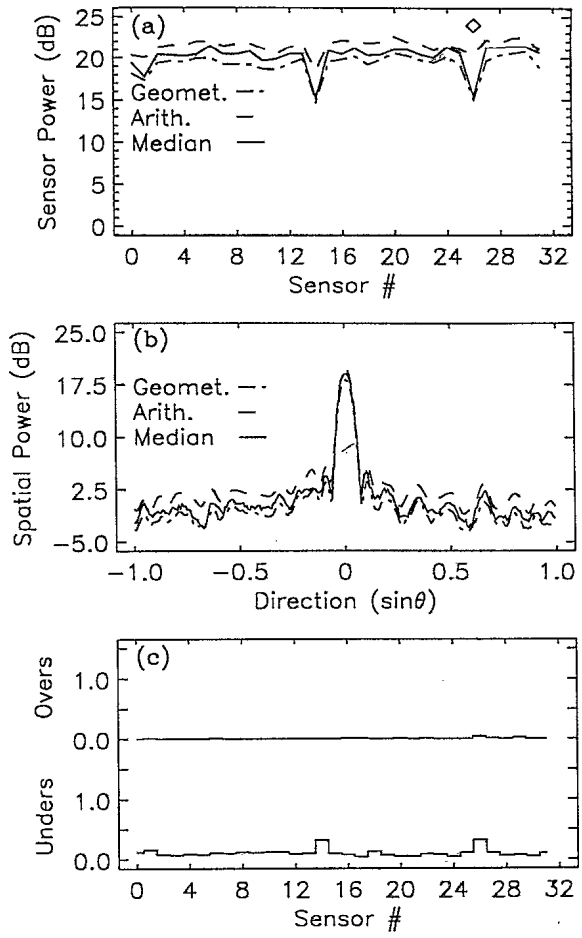

Figure 5. — (a) Plots of arithmetic, geometric, and median mean sensor power estimates as a function of sensor # at bin $k = k_0$. The diamond over sensor 26 indicates the presence of unacceptably high outlier bias. Unacceptable low outlier bias is not observed.; (b); A similar plot as (a) over spatial direction bins. No unacceptable levels of high or low bias are observed; and (c) Fraction of observation period, M, for which over-measurement ("Overs") or under-measurement ("Unders") of $P_F(k_0)$ are observed. Sensors 1, 14, and 26 under-measure more often than the other array sensors. The level of their under-measure is acceptable. The level of over-measure for all sensors is negligible.

5. Fault Synopsis

The existence and location of faults, fault types, and the level of sonar performance degradation related to the faults, may be evaluated with the data provided by the fault analysis process. For these purposes, the demonstration data without the introduction of synthetic faults is considered.

The coherence results of Section 4 indicate that sensors 1, 14, and 26 are completely incoherent. This information is sufficient proof of the existence of sensor faults at these locations. All other sensors are acceptable. As observed from the discrete increases in phase variance for these sensors, there is excessive levels of noise being measured. At this point, the fault type for these sensors appears to be excessive levels of self-noise. By evaluating the parameters of Equation (5), a more detailed picture of the fault type becomes apparent.

To determine the sensor noise at a suspect sensor, i, the smoothing process described in Equation (6) is applied to the temporal arithmetic mean of $P_X(k,i)$ over the range of k. For the purposes of evaluating Equation (5), the level of sensor noise, ${n_i}^2$, relative to $P_{FN}(k_0)$ may be determined by normalizing the previously computed sensor noise value at $k = k_0$ by $P_{FN}(k_0)$. For faulty sensors 1, 14, and 26, this has been measured as 4.55, 2.897, and 3.926, respectively. All other values of ${n_i}^2$ are essentially unity. Except for the identified faulty sensors, the mean phases of adjacent sensors across the aperture are

approximately zero. As sensor phase error becomes irrelevant in a sensor measurement dominated by noise, all sensors can be assumed to have zero phase error for the purposes of evaluating Equation (5). The sensor gain error, G_i, is difficult to determine given an excessively noisy sensor. As the measured powers of the identified faulty sensors are less than that measured by any good sensor in the array (observed from Figure 5 (a)), and the faulty sensors are all excessively noisy, this would indicate that values of G_i for any of the faulty sensors are less than unity. This is an important observation as it implies that the power of the coherent arrival may be severely reduced in the faulty sensors relative to good sensors. As a worst case scenario, the faulty sensors may completely be decoupled from the array. Assuming this is the case, for faulty sensors 1, 14, and 26, $G_i = 0$. For all other good sensors, values of G_i are assumed to be unity.

An evaluation of Equation (5) using these parameters shows an estimated -1.86 dB worst case loss due to the detected faults. This represents a small part of the overall -9.295 dB loss in array gain, tabulated in Section 4. The array gain loss can mostly be attributed to a spatially correlated acoustic noise arrival that significantly reduces noise gain as shown in Table 1. On disassembly of the array it was found that the identified faulty sensors had connector problems and were essentially disconnected from the array.

6. CONCLUSIONS

A hierarchical fault analysis strategy for line-array sonar fault detection and evaluation of fault related performance degradation has been defined and evaluated using real data from a faulty towed line-array. The method is shown to provide a fault detection capability that implicitly locates faults in relation to the array aperture. It is demonstrated that the data resulting from the fault analysis process provides an ability to determine fault type and to evaluate an approximate degradation in sonar performance due to faults. This proposed strategy should be applicable to many other areas where multiple sensors are employed.

7. ACKNOWLEDGMENT

The author would like to recognize the efforts of Dr. I. Fraser for his time in editing, and his valuable comments and suggestions during the course of the work. Also acknowledged are Dr. S. Stergiopoulos, A. Collier, and D. Chapman, for their valuable input during discussion.

8. REFERENCES

[1] M.B. Porter, "Acoustic Models and Sonar Systems," IEEE J. of Oceanic Engineering, vol. 18, no. 4, pp. 425-437, October 1993.

[2] M. Peercy and P. Banerjee, "Fault Tolerant VLSI systems," Proc. IEEE, vol. 81, no. 5, pp. 745-758, May 1993.

[3] R. Isermann, "Process Fault Detection Based on Modeling and Estimation Methods - A survey," Automatica, vol. 20, pp. 387-404, 1984.

[4] R.E. Barlow and F. Proschan, Mathematical Theory of Reliability, New York, Wiley, 1965.

[5] J. Ronen and R.H. Clarke, "Monitoring Techniques for Phased-Array Antennas," IEEE Trans. Antennas Propagat., vol. AP-33, no. 12, pp. 1313-1327, December 1985.

[6] R.A. Wagstaff, J.L. Berrou, F.D. Cotaras, "Use of the Towship for Assessing Towed-Array Performance and Analyzing Data Quality," J. Acoust. Soc. Am., vol. 73, no. 3, pp. 983-992, September 1982.

[7] R.A. Wagstaff, "A Computerized System for Assessing Towed Array Sonar Functionality," IEEE J. of Oceanic Engineering, vol. 18, no. 4, pp. 529-542, October 1993.

#503452